



# Computed entropy spectra for grain boundary segregation in polycrystals

Nutth Tuchinda<sup>1</sup> & Christopher A. Schuh<sup>1,2</sup>✉

Grain boundary solute segregation influences most bulk material properties, and understanding solute thermodynamics at grain boundaries is critical for engineering them. However, the vast grain boundary space in polycrystals is challenging to evaluate due to its size, especially for the intrinsically hard-to-compute segregation excess entropy. Here data science methods are used to generate a database of site-wise grain boundary segregation entropy spectra for 155 dilute binary alloys within the harmonic approximation. The spectral framework allows scale bridging between the calculated atomistic site-wise energy-entropy spectra and macroscopic segregation entropy estimates. The results affirm that macroscopic averaging is not sufficient: a spectral treatment of grain boundary segregation is needed to accurately model bulk temperature dependence of grain boundary solute segregation. The calculated spectral entropy database and thermodynamic framework can be applied for both understanding segregation experiments and alloy design exercises, paving the way to a finite-temperature grain boundary genome.

Tailoring defects is a primary pathway to structure-property engineering in materials<sup>1–6</sup>. In particular, in polycrystalline materials the grain boundaries (GB) constitute a network of disordered regions percolating through the bulk and dominating many properties. Understanding how solute atoms partition to GBs is critical to alloy design due to the ability to control material structure and properties<sup>7–13</sup> via both thermodynamic<sup>14–17</sup> and kinetic<sup>18–21</sup> stabilization of the GBs.

Equilibrium GB segregation states are often modeled with the classical McLean isotherm<sup>22</sup>:

$$\frac{\bar{X}^{\text{GB}}}{1 - \bar{X}^{\text{GB}}} = \frac{X^{\text{C}}}{1 - X^{\text{C}}} \exp \left[ -\frac{\Delta \bar{F}_{\text{eff}}^{\text{seg}}}{k_{\text{B}} T} \right] \quad (1)$$

where  $X^{\text{C}}$  is the solute concentration in the crystals that is in equilibrium with the GB at an average solute concentration  $\bar{X}^{\text{GB}}$ . The free energy of segregation,  $\Delta \bar{F}_{\text{eff}}^{\text{seg}}$  is a combination of the segregation energy and excess entropy of segregation (or the vibrational, magnetic, electronic and other degrees of freedom changes upon solute segregation), i.e.,  $\Delta \bar{F}_{\text{eff}}^{\text{seg}} = \Delta \bar{E}_{\text{eff}}^{\text{seg}} - T \Delta \bar{S}_{\text{eff}}^{\text{seg}}$ . These quantities represent the changes of energy and entropy when the solute segregates from a bulk site to a grain boundary site, and a negative segregation free energy indicates a preference for solute enrichment. The enthalpic term or  $P\Delta V$  is assumed to be small for solids and neglected in this work<sup>23</sup>.

While the simplicity of the McLean isotherm has enabled its usage in a wide range of situations<sup>24–28</sup>, it neglects the atomistic nature of GBs, which involves a broad range of local atomic environments<sup>29–34</sup>. Collapsing the true spectral nature of GB sites to single-value effective quantities in Eq. (1) can cause artificial concentration<sup>31,35</sup>, grain size<sup>36</sup> and temperature dependences<sup>28</sup>; Eq. (1) turns out to be merely a fitting function, and is only valid over the narrow range of concentrations and temperatures for which it is fitted. A better approach to GB segregation is to acknowledge the fundamental physics of GB site competition that defines it, and instead treat grain boundary site equilibrium at site type ' $i$ ' with a local per-site segregation energy ( $\Delta E_i^{\text{seg}}$ ), entropy ( $\Delta S_i^{\text{seg}}$ ), or free energy ( $\Delta F_i^{\text{seg}}$ )<sup>29</sup>:

$$\frac{X_i^{\text{GB}}}{1 - X_i^{\text{GB}}} = \frac{X^{\text{C}}}{1 - X^{\text{C}}} \exp \left[ -\frac{\Delta E_i^{\text{seg}} - T \Delta S_i^{\text{seg}}}{k_{\text{B}} T} \right] = \frac{X^{\text{C}}}{1 - X^{\text{C}}} \exp \left[ -\frac{\Delta F_i^{\text{seg}}}{k_{\text{B}} T} \right] \quad (2)$$

Such calculations for site-wise quantities in polycrystals were not computationally feasible even in the recent past, but due to computational advances, there has been progress in this vein such as the tabulation of  $\Delta E_i^{\text{seg}}$  spectra for a great many alloys based on both interatomic potentials<sup>37</sup> and first principles calculations<sup>38</sup>. Critical to that effort is the use of data science or machine learning methods, which help traverse the many millions of GB sites in a polycrystal.

<sup>1</sup>Department of Materials Science and Engineering, Massachusetts Institute of Technology, 77 Massachusetts Avenue, Cambridge, MA 02139, USA. <sup>2</sup>Department of Materials Science and Engineering, Northwestern University, 2145 Sheridan Road, Evanston, IL 60208, USA. ✉e-mail: [schuh@northwestern.edu](mailto:schuh@northwestern.edu)

The recent availability of GB segregation energy spectra now allows alloy designers to evaluate Eq. (2) for a wide range of dilute binary alloys. However, the site-wise excess entropy,  $\Delta S_i^{\text{seg}}$ , has been mostly neglected and rarely discussed in the past literature due to the extensive computation needed to evaluate it, especially for large polycrystalline structures. Entropic effects cannot generally be neglected at finite temperatures and are considered critical for future alloy design efforts<sup>25,26,39</sup>. The existing literature for this site-wise quantity consists of data for only a few alloy systems and from small coincidence site lattice (CSL) boundaries which cannot fully represent complex grain boundary networks<sup>40–50</sup>.

With recent advances in computation of vibrational entropy using multiscale approaches to the harmonic approximation<sup>45,51–53</sup>, and in the use of data science sampling methods<sup>34,37,38</sup> via local atomic environment descriptors<sup>54,55</sup>, the tools to address GB segregation entropy more broadly are now all in place. We have therefore developed a rapid assessment framework for the polycrystalline  $\Delta E_i^{\text{seg}} - \Delta S_i^{\text{seg}}$  spectra to quantify the extent of vibrational effects using the isotherm of Eq. (2). This is the goal of the present work: to exhaustively explore segregation entropy for common FCC transition metals (Ag-, Al-, Au-, Cu-, Ni-, Pd- and Pt-based alloys) that have published interatomic potentials<sup>56–102</sup>. In addition to providing considerably broader views on the role of entropy in GB segregation, such methods also produce a large quantitative atlas of segregation energy and entropy, for the interpretation of experiments and new efforts in alloy design.

## Results and discussion

### Accelerated model and validation

We first summarize our process in Fig. 1, which begins with site sampling (Fig. 1a–d). Our sampling process is inspired by prior work in which a small number of sites is selected to represent the full distribution of GB sites in a polycrystal<sup>37,38</sup>. Here we begin with a pure solvent  $20 \times 20 \times 20$ -nm polycrystalline structure from ref. 37, then further anneal it using the corresponding interatomic potential, resulting in the structure in Fig. 1a. The GB sites are characterized via local atomic environment (LAE) descriptors, with each LAE vector containing 1015 smooth overlap of atomic positions (SOAP)<sup>54,55</sup> elements (Fig. 1b shows only one example SOAP component). Next, we apply principal component analysis (PCA) for SOAP vector dimensionality reduction as shown in Fig. 1c. The explained-variance ratios

indicate that the 1015 features can be easily collapsed to the first ten PCA components while capturing all the essential features of the local atomic environments.

To sample the site distribution in an efficient and representative manner, we apply K-means clustering to select 500 GB sites for per-site segregation energy (relaxation in Fig. 1e) and entropy calculations (Fig. 1f). We fit segregation energy spectra directly by minimizing negative log-likelihood functions (without, e.g., per-site linear regression with local atomic environments as used elsewhere<sup>37,38</sup>). We show an example of such a segregation energy spectrum in Fig. 1g fitted with a skew-normal distribution with skewness ( $\alpha$ ), position ( $\mu$ ), and size ( $\sigma$ ) parameters<sup>31,103,104</sup>:

$$P_i(\Delta E_i^{\text{seg}}) = \frac{1}{\sqrt{2\pi}\sigma} \exp\left[-\frac{(\Delta E_i^{\text{seg}} - \mu)^2}{2\sigma^2}\right] \text{erfc}\left[\frac{\alpha(\Delta E_i^{\text{seg}} - \mu)}{\sqrt{2}\sigma}\right] \quad (3)$$

For the site entropy distribution, we employ additional methods. For the 500 sites selected above, we perform the excess entropy calculation from ref. 51 based on a full harmonic calculation around the solute site, coupled to a local harmonic approximation<sup>45,53,105</sup> at greater distances, an approach that balances computational efficiency with accuracy (details are listed in Method and Supplementary Material 1). We then calculate sample means ( $\mu$ ) and covariance matrices ( $\Sigma$ ) amongst the energies and entropies of the sampled sites, casting the full distribution as a bivariate Gaussian:

$$P_i(\mathbf{x} = [\Delta E_i^{\text{seg}}, \Delta S_i^{\text{seg}}]) = \frac{1}{2\pi\sqrt{|\Sigma|}} \exp\left[-\frac{1}{2}(\mathbf{x} - \boldsymbol{\mu})^T \Sigma^{-1}(\mathbf{x} - \boldsymbol{\mu})\right] \quad (4)$$

In Fig. 1h, we plot an example kernel density estimate for the segregation energy and entropy from 500 GB sites for Ni(Zr)<sup>102</sup>.

An important feature of the distribution in Fig. 1h is that there is a correlation between site energy and entropy; this is known as the ‘compensation effect’ in literature on GB segregation<sup>106</sup>. As we have demonstrated in ref. 51, this correlation permits substantial simplification of the mathematics of Eq. (2), because it allows information about site energy (which is easily computed) to be projected into information about site entropy (which is not). Such mapping can be conducted accurately with a

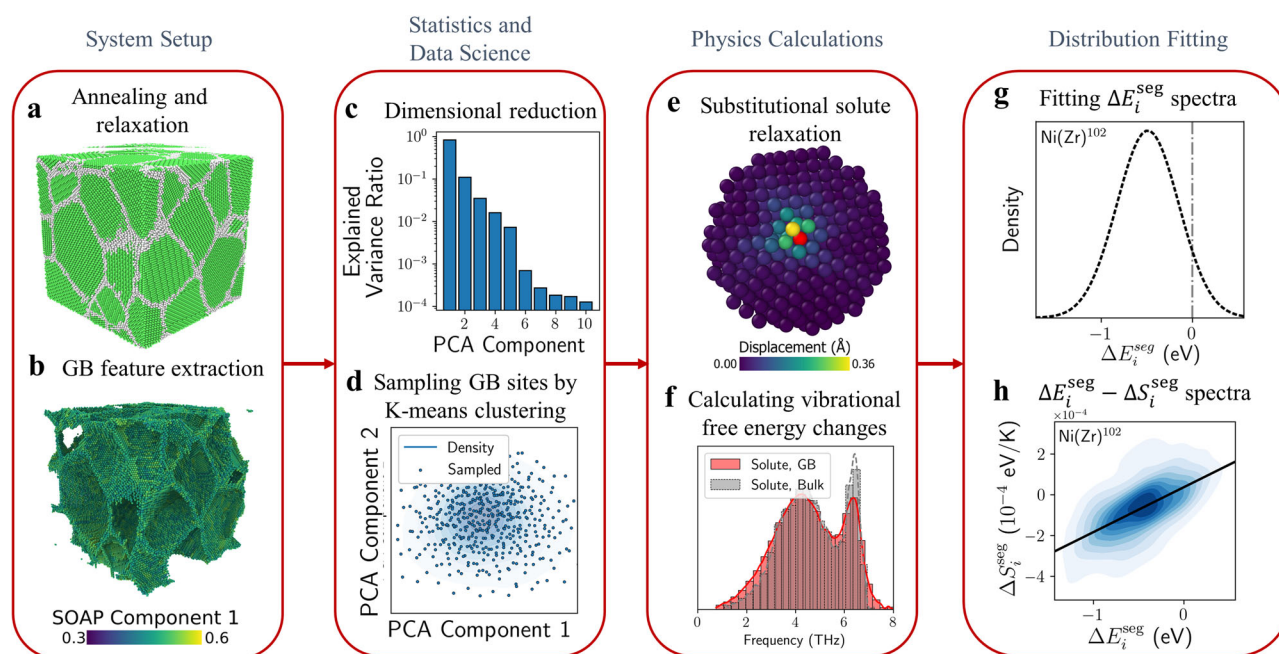


**Fig. 1 | Entropy estimation workflow.** **a** The polycrystals used in this work were obtained from the database in ref. 37 and further annealed and relaxed. **b** SOAP feature vectors are constructed for grain boundary site samplings via principal

component analysis<sup>140–142</sup> **c** and sampled via K-means clustering<sup>143,144</sup> **d**. The sites near K-means centers are used to calculate substitutional segregation energy **e** and vibrational entropy **f** for spectral fitting in **g** and **h**, exemplified here for Ni(Zr)<sup>102</sup>.

linear energy-entropy compensation<sup>40,51</sup>:

$$\Delta S_i^{\text{seg}} = \chi \Delta E_i^{\text{seg}} + \Delta S_0^{\text{solute,GB}} \quad (5)$$

where  $\chi$  and  $\Delta S_0^{\text{solute,GB}}$  are system-specific parameters that characterize the correlation between site energy and entropy, and which we can aspire to tabulate for many materials. Typically, in correlated systems such as this, sample correlations stabilize close to the true population value when conducting random sampling at less than  $N = 500^{107}$ ; we use  $N = 500$  and the application of K-means clustering should converge more quickly than random sampling, so we expect high accuracy for the estimation of  $\chi$  and  $\Delta S_0^{\text{solute,GB}}$ . To validate this expectation we report root mean squared errors (RMSE) of this approach with respect to a randomly sampled 500-site validation set in Supplementary Material 3.

Having established the framework in Fig. 1, we turn our attention to validating the accelerated model against full spectra computed exhaustively on full polycrystals. We show example spectra for a  $13 \times 13 \times 13$ -nm Ni(Pt)<sup>58</sup> system in Fig. 2a. The full lines in blue represent the 500-sample distribution derived from the accelerated sampling model, plotted atop the dashed lines corresponding to the full spectrum of about 50,000 GB sites; the agreement is very good. The projected spectra, on both the energy and entropy axes, also show good agreement between the two. In a practical sense, spectra such as these provide all the information needed for a rigorous prediction of grain boundary segregation for dilute alloys, which can be encoded in the form of the distribution functions. In the large grain size limit ( $X^C \approx X^{\text{tot}}$ , the total system solute content), grain boundary concentration can be evaluated by integrating the site density function of Eq. (4) weighted by local concentration ( $X_i^{\text{GB}}$ ) of Eq. (2):

$$\bar{X}^{\text{GB}} = \int \int d\Delta E_i^{\text{seg}} d\Delta S_i^{\text{seg}} P_i X_i^{\text{GB}} \quad (6)$$

In Fig. 2b, we show outputs of such calculations estimated from the spectra in Fig. 2a for 1 at.% solute loading, and demonstrate the similarity between the accelerated and full spectrum. We have performed this kind of exhaustive validation for several Ni-based systems (Pd, Ag, Au, and Cu), and obtained reasonable accuracy of grain boundary concentrations as shown in Supplementary Material 1 (errors are below 5% relative to the full spectra).

With this validation we proceed with confidence in the methods, and turn our attention to the assessment of the spectra for dilute FCC binary alloys for which there are published interatomic potentials<sup>56-102</sup>. More details of the method are described in the method section and Supplementary Material 1. The segregation energy spectra are listed in Supplementary Material 2, and the energy-entropy spectra are listed in

Supplementary Material 3. The dataset shown in this work is published in the repository<sup>108</sup>.

### Segregation energy and entropy spectra

A major outcome of the workflow in Fig. 1 is that we can now very quickly estimate full, polycrystalline grain boundary segregation spectra, inclusive of both energy and entropy terms, with just a small number of computations on true polycrystals, amplified by data science principles. As an example, we show the full spectra for several Cu-based systems in Fig. 3. This includes systems with a wide range of behaviors, with different distribution centers, different widths and different degrees of energy-entropy correlation ( $\rho$ ). The spectra for all of the systems explored in this work are presented in Supplementary Material 2, 3, along with the bivariate normal fitting parameters that allow reconstruction of the full distribution on the basis of Eq. (4). This collection of 155 binary GB segregation spectra is one of the most exhaustive of its kind, and should permit detailed comparison with experimental data, new efforts in alloy design, and, as we shall see below, further commentary on the nature of excess entropy in grain boundary segregation problems.

One challenge with GB segregation spectra generally is that their accuracy is only as great as that of the interatomic potentials from which they derive. Taking Cu(Ag) as an example binary system, we show  $\Delta E_i^{\text{seg}} - \Delta S_i^{\text{seg}}$  spectra from three different interatomic potentials<sup>58,60,61</sup> proposed in the literature in Fig. 4a–c. Their corresponding isotherms at 1 at.% total solute content as a function of temperature are calculated via Eq. (4) and plotted in Fig. 4d–f, both with and without site-wise excess entropies. These isotherms depict how site-wise spectra unfold into the average GB concentrations often measured in experiments, and to what extent vibrational entropic effects play a role in grain boundary segregation (or i.e., the ratio between  $\bar{X}_{w/\Delta S_i^{\text{seg}}}^{\text{GB}}$  and  $\bar{X}_{w/\Delta S_i^{\text{seg}}}^{\text{GB}}$ ). The spectra along with the isotherm solver in the Supplementary Material can be used to calculate a dilute isotherm of interest. However, the results in Fig. 4 also provide a note of caution about any results based on the use of interatomic potentials, as the three nominally identical alloys in Fig. 4 have rather different predicted GB segregation spectra, and expect different levels of GB solute enrichment as a result. The inclusion of disordered structures in, for instance, metallic glass and grain boundary potentials, and other more accurate methods such as machine learning potentials<sup>109,110</sup> may yield more accurate forces required for accurate entropy calculations.

### The Importance of excess entropy on segregation

Although it is common to neglect excess entropy in GB segregation analysis, this is generally only appropriate at the lowest temperatures. The present survey of many alloy systems highlights the fact that there are significant

**Fig. 2 | Validating the accelerated model.** Segregation energy-entropy spectrum of Ni(Pt)<sup>58</sup> obtained from the accelerated model and a full  $13 \times 13 \times 13$ -nm system are plotted atop one another for comparison in **a**. The spectra can be well modeled with a bivariate Gaussian distribution and used to calculate the GB concentrations shown in **b** in the large grain size limit with  $X^{\text{tot}} = 1$  at.%.

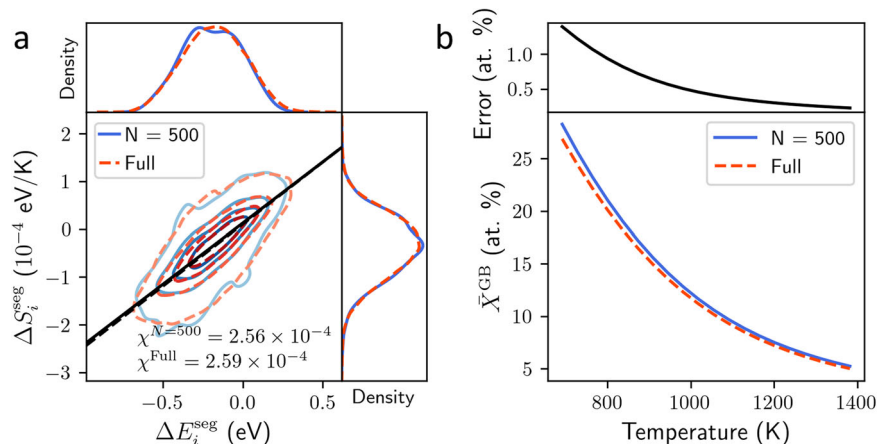


**Fig. 3 | Energy-entropy grain boundary spectra of Cu-based alloys.** Density plots of solute segregation energy and excess vibrational entropy from the accelerated model of Fig. 1 are shown for the systems with the largest correlation ( $\rho$ ) or energy-entropy ‘compensation effect’ for a given solute. See Supplementary Material 3 for the full data for all systems, and fitting parameters that can be used to reproduce these distributions.

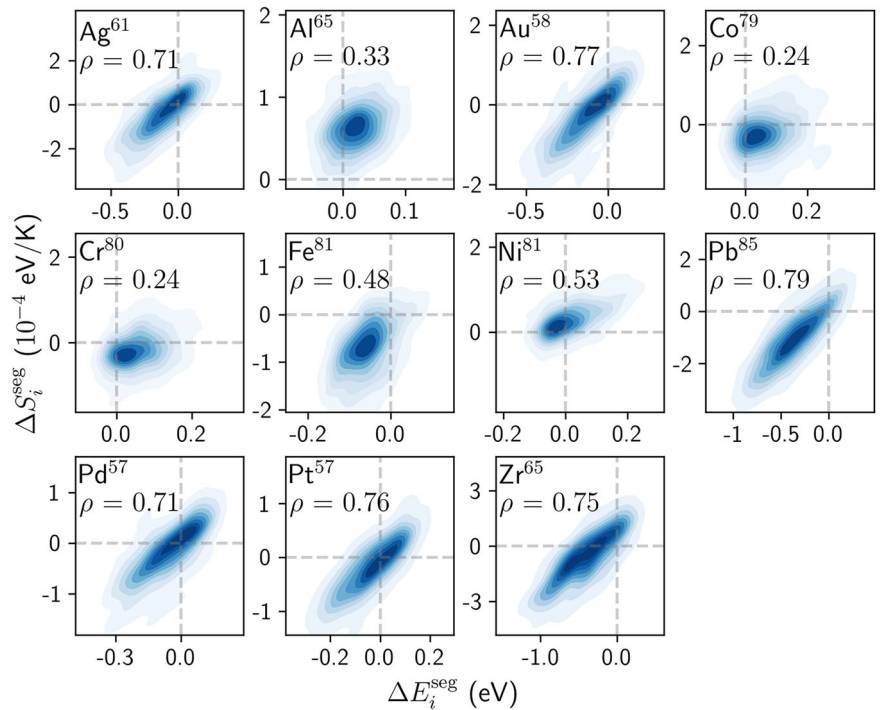
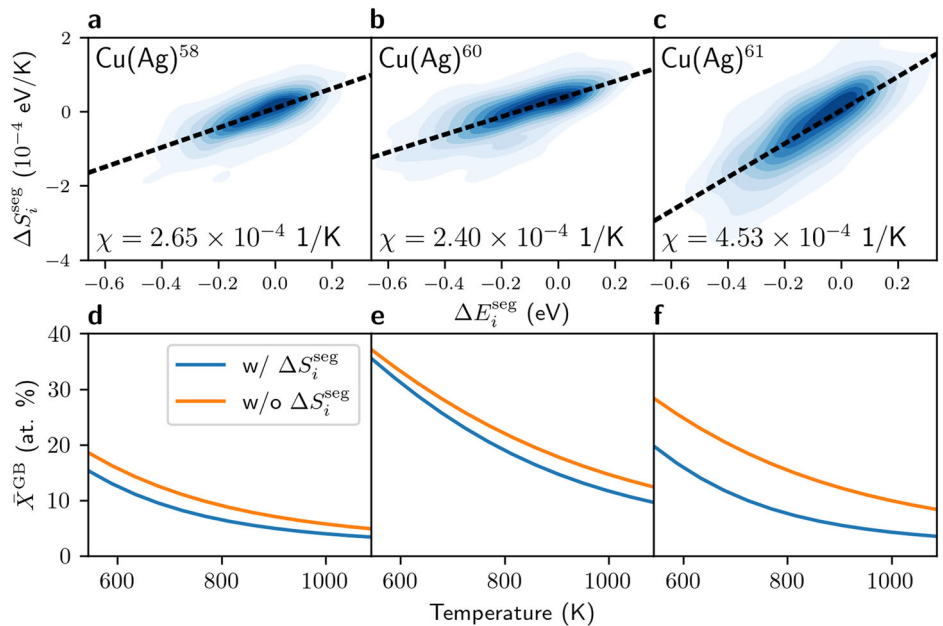


**Fig. 4 | Cu(Ag) segregation behavior.** Spectra for three Cu(Ag) systems<sup>58,60,61</sup> based on different published interatomic potentials are shown in a–c with their corresponding spectral segregation isotherm in d–f both with and without excess entropies. The choice of potential has a significant impact on the output of segregation models, especially as regards the site excess entropy and the compensation effect. See Supplementary Material 3 for the full spectral information.



entropic contributions due to the spectrality of GB site free energies. This is apparent in the Cu(Ag) system shown in Fig. 4 where in Fig. 4f the GB concentration can be much lower due to the compensation effects which penalize the negative tail of segregation distribution<sup>51</sup>, and thus affect how solute redistributes with increasing temperature<sup>31</sup>. To amplify this point, in Fig. 5, we show the isotherm normalized errors,  $\beta$ , defined as:

$$\beta = \left| \bar{X}_{w/\Delta S_i^{\text{seg}}}^{\text{GB}} - \bar{X}_{w/o\Delta S_i^{\text{seg}}}^{\text{GB}} \right| / \bar{X}_{w/\Delta S_i^{\text{seg}}}^{\text{GB}} \quad (7)$$

where  $\bar{X}_{w/\Delta S_i^{\text{seg}}}^{\text{GB}}$  and  $\bar{X}_{w/o\Delta S_i^{\text{seg}}}^{\text{GB}}$  indicate equilibrium grain boundary solute concentration predicted with and without excess entropies in Eq. (2). This quantity,  $\beta$ , is essentially the relative contribution of excess entropy to the grain boundary concentration. The figure shows that excess entropy is very

important to accurate predictions: even at moderate temperatures, most systems differ more than ~15% (medians lie above 0.15 in Fig. 5) from the true segregation state. At higher temperatures where entropy becomes more important, this error becomes much higher, with some cases having more than 100% error at  $\beta > 1$ . There are several edge cases in the uppermost quartile such as Cu(Ag) in Fig. 4f for which GB concentrations can be overestimated by more than a factor of two, affecting alloy design criteria such as nanocrystalline stability<sup>111,112</sup>.

### Grain boundary segregation spectra and enthalpy-entropy relationship

In prior works<sup>40,51</sup>, per-site GB segregation energy and entropy have been found to be strongly correlated for a few dilute Ni-based systems, as

suggested by the compensation effect of Eq. (5). With more access to data for 155 alloy systems, the present work permits evaluation of that linear relationship more broadly. Looking at the example Cu-based systems in Fig. 3, we find that essentially all systems exhibit positive correlations of the kind

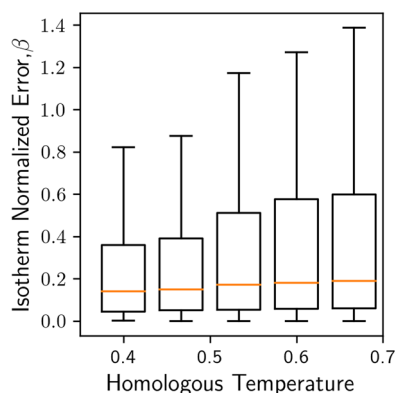


**Fig. 5 | Excess entropic effects in GB segregation prediction.** A boxplot showing the distribution of all 155 alloy systems and the importance of excess site entropy on GB segregation; the y-axis shows the isotherm prediction errors when excess entropies are excluded, normalized by the GB concentration predicted with excess entropies. For this computation the bulk concentration is taken as 1 at.% in the large grain limit (i.e.,  $X^C \approx X^{tot}$ ). The box lower and upper bounds denote the first and third quartiles respectively, with the centerlines representing the medians. The whiskers extend by 1.5 times the interquartile range beyond the box bounds.

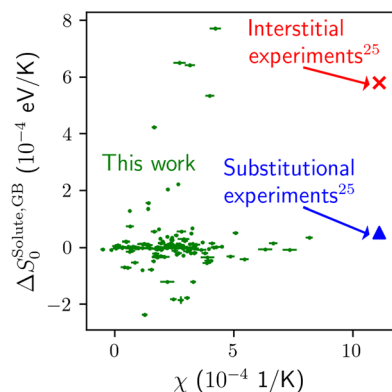


**Fig. 6 | Atomistic vis-à-vis macroscopic compensation effects.** Atomistic compensations ( $\chi$  and  $\Delta S_0^{Solute,GB}$ ) are plotted along with the macroscopic compensation slopes and intercepts from ref. 25 estimated from multiple substitutional and interstitial solute segregation in  $\alpha$ -iron summarized in refs. 162,163. Error bars for 155 atomistic  $\chi$  and  $\Delta S_0^{Solute,GB}$  are calculated from 80% sample bootstrapping.

expected; all of the distribution functions slant at least somewhat to the right. Some of the interatomic potentials show quite high correlations (two-thirds of the example systems in Fig. 3 have  $\rho > 0.7$ ); the other systems such as Cu(Al)<sup>65</sup>, Cu(Co)<sup>96</sup> and Cu(Cr)<sup>80</sup> are exceptions, with correlations as low as 0.24.

Looking at all of the systems represented in Supplementary Material 3, we find that positive energy-entropy correlations are indeed typical; the only exceptions of Ni(Co)<sup>91</sup> and Ni(Cu)<sup>82</sup> are essentially uncorrelated and by happenstance can be fitted with a slightly negative slope with a low magnitude of order  $\chi \sim 10^{-5}$  1/K, suggesting negligible excess entropies in both systems. The generally positive correlations are in agreement with the previously reported data for both atomistic simulations<sup>40,113,114</sup> and experimentally-realized macroscopic compensation effects<sup>26,115</sup>.

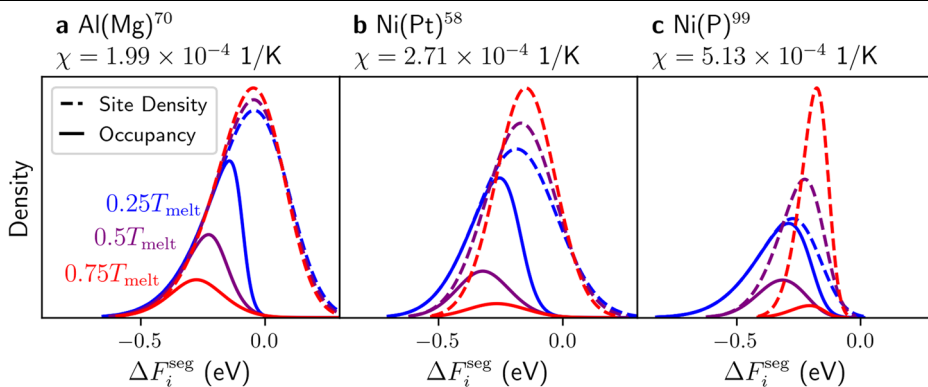
The energy-entropy compensation effect has been discussed in an experimental context by using the classical McLean isotherm of Eq. (1) and fitting it to experimental measurements of GB segregation for many materials<sup>26,115</sup>. The result is indeed a linear correlation of the form of Eq. (5), not in a site-wise fashion, but as a broad average trend across the literature; see for example the review in ref. 25. The availability of site-wise data for 155 alloys permits a first comparison of the aggregated trends across all alloys, which we perform in Fig. 6. Here we plot all 155  $\chi$  and  $\Delta S_0^{Solute,GB}$  (i.e., the compensation slope and intercept, respectively) from all the present computed alloy systems, along with those from the aggregated experimental literature data from ref. 26. There are two slopes representing experimental data, as there are two clusters of results in the literature, which have been suggested to correspond to substitutional (blue  $\blacktriangle$ ) and interstitial (red  $\times$ ) GB segregation, respectively, in Fe-based alloys. Note that the present computations are strictly based on substitutional segregation, although it is instructive to see both substitutional and interstitial experimental trends in Fig. 6.

The comparison in Fig. 6 suggests a rather remarkable disagreement: the site-wise compensation slope for a given system is often an order of magnitude lower than the experimental McLean effective energy-entropy compensation ( $\sim 10^{-4}$  1/K for per-site spectra vis-à-vis  $\sim 10^{-3}$  1/K for bulk substitutional compensation in refs. 25,116). In other words, the experimental data predict substantially higher entropic effects and associated temperature dependences of GB segregation (if applied to any single site). This disagreement is caused by a mathematical artifact in the use of Eq. (1) with experimental data: the collapsing of spectral GB quantities to a single effective McLean segregation energy is known to result in artificial temperature dependences of the fitted segregation quantities<sup>28,117</sup>. When Eq. (1) is fitted to experimental data, the effective segregation enthalpies and entropies, in turn, produce artificially large compensation effects; the neglect of spectrality misses the true physics of temperature-dependent site selection, and in turn requires artificially high ‘average’ entropies in order to fit the data.

Thus, at the atomic site-level, the true ‘compensation effect’ in GB segregation is remarkably small compared to expectations based on prior experimental literature. By extension, it is also somewhat surprising how important that very small compensation effect is: we still observe many

**Fig. 7 | Solute occupancy of segregation spectra.**

The density of segregation sites is shown (on the basis of full free energies) as a function of temperature (dashed lines), as well as the solute occupancy of those sites (site density times local concentration  $X_i^{GB}$ ) for 1% solute content in a–c. Spectra are shown for **a** Al(Mg)<sup>70</sup>, **b** Ni(Pt)<sup>58</sup> and **c** Ni(P)<sup>99</sup>, which have three quite different values of the energy-entropy compensation parameter  $\chi$ , whose effects penalize the negative tail of the distributions.



systems with drastic entropic effects in Fig. 5. This occurs because the role of entropy is more complex in a spectral system, affecting which sites are occupied in subtle ways, and preferentially compensating the negative tail of the segregation energy distribution. For demonstration we show how solute atoms occupy Al(Mg)<sup>70</sup>, Ni(Pt)<sup>58</sup> and Ni(P)<sup>99</sup> grain boundaries in Fig. 7a–c respectively. These three systems represent three different magnitudes of the compensation slope  $\chi$ . Al(Mg) in 7a has a small  $\chi$  and a low melting point, resulting in near-constant free energy distributions with temperature. As a result, the negative tail is populated at all temperatures, and hence there are negligible entropic effects. Conversely, there is very strong compensation of the negative tails in 7b and 7c as temperature rises for the systems with moderate (Ni(Pt)<sup>58</sup>) to large  $\chi$  (Ni(P)<sup>99</sup>). The most energetic segregation sites simply disappear due to the strong effects of site entropy, leading to very strong temperature dependence of segregation, and thus very high apparent segregation entropy of the system on average. This effect of the shifting free energy spectrum lies at the heart of the discrepancy between theory and experiment in Fig. 6: the lack of a spectrum in the experimental data analysis requires the use of a multifold inflation on the role of excess entropy.

The results in Figs. 6 and 7 provide a note of caution in the use of averaged quantities for GB segregation problems; neglecting the full spectral nature of the problem can give energy and entropy quantities that are off significantly from the true, physical values they are expected to have. This calls for innovation in the approach to interpreting GB segregation experiments. Such experiments are not trivial, and fitting just a single segregation spectrum requires tremendous experimental data<sup>18</sup>. With recent advances in nanoscale resolution characterization tools<sup>119–124</sup> and the spectral framework now better established<sup>29,31,51</sup>, we hope that both future experimental effort and more accurate free energy estimations will allow us to accurately determine spectra of GB segregation. A similar note of caution should be applied to the theoretical viewpoint as well; although spectral forms like the ones used here have a sound physical motivation, they too can miss important details relevant to the interpretation of experiments. For example, the framework and results presented here are limited to dilute limit segregation within the harmonic approximation. Anharmonicity may become large, and grain boundary structural transformations and complexion energies may play major roles at high temperatures<sup>124–130</sup>. Solute-solute interactions are not discussed here, but should in principle also be included via the frameworks described elsewhere<sup>35,131,132</sup>. Thus, the significant gap between experiment and theory in Fig. 6 needs more concerted attention from both the experimental and theoretical points of view, but clearly should be resolved with a spectral view of segregation.

In summary, dilute polycrystalline grain boundary segregation vibrational entropy spectra have been estimated and tabulated for 16 Ag, 22 Al, 10 Au, 35 Cu, 51 Ni, 11 Pd and 10 Pt-based binary alloys. These entropy spectra are very dependent on the fitting of the corresponding interatomic potential, but in aggregate they speak to a positive correlation between segregation energy and excess entropy as expected physically. These energy-entropy compensation slopes are mostly positive in agreement with the past theoretical literature. However, the spectra here show large discrepancies compared to experimental compensation effects; the experiments unfortunately have strong artificial entropic effects from neglecting the spectrality of segregation energy and entropy, instead forcing a fit with average or effective thermodynamic quantities. This work thus significantly encourages the usage of spectral isotherm models for more accurate descriptions of GB segregation.

## Methods

### Polycrystalline structures

To quantify segregation energy and vibrational entropy of intergranular site solute segregation, we use the polycrystals published in refs. 38,133. We anneal at 0.4 of the melting temperature for 100 ps then quench to 0 K at 2 K/ps via Nose-Hoover thermostat/barostat at zero pressure followed by relaxation with the FIRE<sup>134,135</sup> algorithm, using as termination criterion that the force norm of all atoms lies below  $10^{-6}$  eV/Å. Both annealing and

relaxation are conducted using the Large-scale Atomic/Molecular Massively Parallel Simulator (LAMMPS) software package<sup>136–139</sup>.

### Statistical and data science framework

After obtaining the base elemental polycrystals, we follow a statistical procedure in the spirit of refs. 37,38. We first characterize atoms using the smooth overlap of atomic positions (SOAP) descriptor via QUIPPY<sup>54,55</sup> with  $r_{\text{SOAP}}^{\text{cut}} = 6 \text{ \AA}$ ,  $n^{\text{max}} = l^{\text{max}} = 12$  and Gaussian width  $\sigma_{\text{SOAP}} = 1 \text{ \AA}$ , resulting in 1015 SOAP features. Dimensionality reduction is carried out with principal component analysis<sup>140–142</sup>. K-means clustering<sup>143,144</sup> is then applied to sample 500 sites for calculating segregation energy and vibrational entropy. Ten bulk sites are chosen randomly from amongst those sites more than 3 nm from any grain boundary site identified by Adaptive Common Neighbor Analysis<sup>145,146</sup> implemented in the OVITO software package<sup>147</sup>.

### Vibrational entropy estimation

We employ the multiscale algorithm developed in our previous work of ref. 51. The free energy is calculated via<sup>43,45,53</sup>:

$$F = U_0 + k_B T \sum_i^{3N} \ln \left[ 2 \sinh \left( \frac{h\nu_i}{2k_B T} \right) \right] \quad (8)$$

with  $U_0$  the potential energy from the interatomic potential and the summation conducted over the eigenvalues obtained from dynamical matrices calculated with LAMMPS<sup>148,149</sup> and  $T = 0.6T_{\text{melt}}$ . Vibrational free energy of segregation is defined via the double difference:

$$\Delta F_{\text{vib},i}^{\text{seg}} = \left( F_{\text{GB},i}^{\text{solute}} - F_{\text{GB},i}^{\text{pure}} \right) - \left( F_{\text{bulk}}^{\text{solute}} - F_{\text{bulk}}^{\text{pure}} \right) - \Delta E_i^{\text{seg}} \quad (9)$$

where superscripts ‘solute’ and ‘pure’ denote whether the site is occupied by a solute or a solvent atom. The subscript indicates the site (GB, ‘i’ for a GB site type  $i$  and ‘bulk’ from the average of 10 bulk sites). We include details of such calculations in Supplementary Material 1. Note that while the entropy changes of harmonic oscillators converge at high temperatures, there could be anharmonicity, volumetric effects and grain boundary transitions not incorporated in this study<sup>43,51,126,129</sup>.

### Spectral segregation isotherm

A Jupyter notebook is implemented with the Python libraries<sup>103,150–159</sup> and is provided for readers to calculate segregation isotherms equivalent to Figs. 4 and 5 for the tabulated alloys. At finite grain sizes, the following solute balance equation is solved<sup>160</sup>:

$$X^{\text{tot}} = (1 - f^{\text{GB}})X^{\text{C}} + f^{\text{GB}}\bar{X}^{\text{GB}} \quad (10)$$

where  $\bar{X}^{\text{GB}}$  can be calculated via the isotherm of Eq. (2) with the rearranged form of  $X_i^{\text{GB}}$ :

$$\bar{X}^{\text{GB}} = \int \int d\Delta E_i^{\text{seg}} d\Delta S_i^{\text{seg}} P_i(\Delta E_i^{\text{seg}}, \Delta S_i^{\text{seg}}) \left[ 1 + \frac{1-X^{\text{C}}}{X^{\text{C}}} \exp \left( \frac{\Delta E_i^{\text{seg}} - T\Delta S_i^{\text{seg}}}{k_B T} \right) \right]^{-1} \quad (11)$$

and  $f^{\text{GB}}$  is the grain boundary atomic fraction which scales with grain sizes ( $d$ )<sup>36,161</sup>. The commonly used form of  $f^{\text{GB}}$  is:

$$f^{\text{GB}} = 1 - \left( \frac{d-t}{d} \right)^3 \quad (12)$$

with  $t$  as the grain boundary thickness. We note that with increasing temperature,  $\Delta S_i^{\text{seg}}/k_B$  becomes significant vis-à-vis  $\Delta E_i^{\text{seg}}/k_B T$  and hence alters solute equilibrium at finite temperatures. The isotherms used here also neglect solute-solute interactions and short-range ordering at grain boundaries.

Details on numerical implementations can be found in Supplementary Material 4. The large grain limit of Eq. (11) is used throughout the paper without the finite size correction of Eqs. (10) and (12). The finite GB form is included in the supplemental Jupyter notebook for use with nanocrystalline alloys.

### Data availability

Calculated segregation energies and entropies along with their corresponding polycrystalline structure are available on the repository<sup>108</sup>.

### Code availability

A notebook for integrating the isotherm of Eqs. (10–12) is included in the Supplementary Material. A notebook for processing the dataset is included in the repository<sup>108</sup>.

Received: 13 September 2023; Accepted: 29 March 2024;

Published online: 12 April 2024

### References

- Hansen, N. Hall–Petch relation and boundary strengthening. *Scr. Mater.* **51**, 801–806 (2004).
- Uberuaga, B. P., Vernon, L. J., Martinez, E. & Voter, A. F. The relationship between grain boundary structure, defect mobility and grain boundary sink efficiency. *Sci. Rep.* **5**, 9095 (2015).
- Eswarappa Prameela, S., Yi, P., Falk, M. L. & Weihs, T. P. Strategic control of atomic-scale defects for tuning properties in metals. *Nat. Rev. Phys.* **3**, 148–149 (2021).
- Suzuki, A., Inui, H. & Pollock, T. M. L1<sub>2</sub>-strengthened cobalt-base superalloys. *Annu. Rev. Mater. Res.* **45**, 345–368 (2015).
- Randle, V. Twinning-related grain boundary engineering. *Acta Mater.* **52**, 4067–4081 (2004).
- Liu, T.-C., Liu, C.-M., Huang, Y.-S., Chen, C. & Tu, K.-N. Eliminate Kirkendall voids in solder reactions on nanotwinned copper. *Scr. Mater.* **68**, 241–244 (2013).
- Rofagha, R., Erb, U., Ostrander, D., Palumbo, G. & Aust, K. The effects of grain size and phosphorus on the corrosion of nanocrystalline Ni–P alloys. *Nanostruct. Mater.* **2**, 1–10 (1993).
- Pun, S. C. et al. Nanocrystalline Al–Mg with extreme strength due to grain boundary doping. *Mater. Sci. Eng. A* **696**, 400–406 (2017).
- Rupert, T. J., Trenkle, J. C. & Schuh, C. A. Enhanced solid solution effects on the strength of nanocrystalline alloys. *Acta Mater.* **59**, 1619–1631 (2011).
- Hofmann, S. & Lejček, P. Solute segregation at grain boundaries. *Interface Sci.* **3**, 241–267 (1996).
- Kuzmina, M., Ponge, D. & Raabe, D. Grain boundary segregation engineering and austenite reversion turn embrittlement into toughness: example of a 9wt.% medium Mn steel. *Acta Mater.* **86**, 182–192 (2015).
- Lejček, P. & Hofmann, S. Thermodynamics and structural aspects of grain boundary segregation. *Crit. Rev. Solid State Mater. Sci.* **20**, 1–85 (1995).
- Raabe, D. et al. Grain boundary segregation engineering in metallic alloys: a pathway to the design of interfaces. *Curr. Opin. Solid State Mater. Sci.* **18**, 253–261 (2014).
- Weissmüller, J. Alloy effects in nanostructures. *Proc. First Int. Conf. Nanostruct. Mater.* **3**, 261–272 (1993).
- Kirchheim, R. Grain coarsening inhibited by solute segregation. *Acta Mater.* **50**, 413–419 (2002).
- Trelewicz, J. R. & Schuh, C. A. Grain boundary segregation and thermodynamically stable binary nanocrystalline alloys. *Phys. Rev. B* **79**, 094112 (2009).
- Chookajorn, T., Murdoch, H. A. & Schuh, C. A. Design of stable nanocrystalline alloys. *Science* **337**, 951–954 (2012).
- Hillert, M. Solute drag, solute trapping and diffusional dissipation of Gibbs energy<sup>11</sup>This paper is based on the Hume–Rothery Lecture presented at the 128th TMS Annual Meeting, 1 March 1999, San Diego, U.S.A. *Acta Mater.* **47**, 4481–4505 (1999).
- Hillert, M. Solute drag in grain boundary migration and phase transformations. *Acta Mater.* **52**, 5289–5293 (2004).
- Kim, S. G. & Park, Y. B. Grain boundary segregation, solute drag and abnormal grain growth. *Acta Mater.* **56**, 3739–3753 (2008).
- Alkayyali, M. & Abdeljawad, F. Grain boundary solute drag model in regular solution alloys. *Phys. Rev. Lett.* **127**, 175503 (2021).
- McLean, D. *Grain Boundaries in Metals* (Clarendon Press, 1957).
- Lejček, P., Zheng, L., Hofmann, S. & Šob, M. Applied Thermodynamics: Grain Boundary Segregation. *Entropy* **16**, 1462–1483 (2014).
- Sutton, A. P. & Balluffi, R. W. *Interfaces in Crystalline Materials*. (OUP Oxford, 2006).
- Lejček, P. & Hofmann, S. Entropy-driven grain boundary segregation: prediction of the phenomenon. *Metals* **11**, 1331 (2021).
- Lejček, P., Hofmann, S. & Paidar, V. The significance of entropy in grain boundary segregation. *Materials* **12**, 492 (2019).
- Hondros, E. D. & Seah, M. P. The theory of grain boundary segregation in terms of surface adsorption analogues. *Metall. Trans. A* **8**, 1363–1371 (1977).
- Scheiber, D., Romaner, L., Pippan, R. & Puschnig, P. Impact of solute–solute interactions on grain boundary segregation and cohesion in molybdenum. *Phys. Rev. Mater.* **2**, 093609 (2018).
- White, C. & Stein, D. Sulfur segregation to grain boundaries in Ni 3Al and Ni 3 (Al, Ti) alloys. *Metall. Trans. A* **9**, 13–22 (1978).
- Patala, S. Understanding grain boundaries—the role of crystallography, structural descriptors and machine learning. *Comput. Mater. Sci.* **162**, 281–294 (2019).
- Wagih, M. & Schuh, C. A. Spectrum of grain boundary segregation energies in a polycrystal. *Acta Mater.* **181**, 228–237 (2019).
- Homer, E. R., Hensley, D. M., Rosenbrock, C. W., Nguyen, A. H. & Hart, G. L. W. Machine-learning informed representations for grain boundary structures. *Front. Mater.* **6**, 168 (2019).
- Mahmood, Y., Alghalayini, M., Martinez, E., Paredis, C. J. J. & Abdeljawad, F. Atomistic and machine learning studies of solute segregation in metastable grain boundaries. *Sci. Rep.* **12**, 6673 (2022).
- Huber, L., Hadian, R., Grabowski, B. & Neugebauer, J. A machine learning approach to model solute grain boundary segregation. *Npj Comput. Mater.* **4**, 64 (2018).
- Wagih, M. & Schuh, C. A. Grain boundary segregation beyond the dilute limit: separating the two contributions of site spectrality and solute interactions. *Acta Mater.* **199**, 63–72 (2020).
- Tuchinda, N. & Schuh, C. A. Grain size dependencies of intergranular solute segregation in nanocrystalline materials. *Acta Mater.* **226**, 117614 (2022).
- Wagih, M., Larsen, P. M. & Schuh, C. A. Learning grain boundary segregation energy spectra in polycrystals. *Nat. Commun.* **11**, 6376 (2020).
- Wagih, M. & Schuh, C. A. Learning grain-boundary segregation: from first principles to polycrystals. *Phys. Rev. Lett.* **129**, 046102 (2022).
- Fultz, B. Vibrational thermodynamics of materials. *Prog. Mater. Sci.* **55**, 247–352 (2010).
- Rittner, J. D. & Seidman, D. N. Solute-atom segregation to <110>-symmetric tilt grain boundaries. *Acta Mater.* **45**, 3191–3202 (1997).
- Rittner, J. D., Udler, D., Seidman, D. N. & Oh, Y. Atomic scale structural effects on solute-atom segregation at grain boundaries. *Phys. Rev. Lett.* **74**, 1115–1118 (1995).
- Rittner, J. D., Udler, D. & Seidman, D. N. Solute-atom segregation at symmetric twist and tilt boundaries in binary metallic alloys on an atomic-scale. *Interface Sci.* **4**, 65–80 (1997).
- Creuze, J., Berthier, F., Tétot, R., Legrand, B. & Tréglia, G. Intergranular segregation and vibrational effects: a local analysis. *Phys. Rev. B* **61**, 14470–14480 (2000).

44. Creuze, J., Berthier, F., Tétot, R. & Legrand, B. Intergranular segregation and ordering effect: a mixed Monte Carlo mean-field approach. *Phys. Rev. B* **62**, 2813–2824 (2000).
45. Najafabadi, R., Wang, H. Y., Srolovitz, D. J. & Lesar, R. A new method for the simulation of alloys: application to interfacial segregation. *Acta Metall. Mater.* **39**, 3071–3082 (1991).
46. Wang, H. Y., Najafabadi, R., Srolovitz, D. J. & Lesar, R. Segregation to  $\Sigma 5$  [001] twist grain boundaries in ni-cu alloys. *Philos. Mag. A* **65**, 625–655 (1992).
47. Wang, H. Y., Najafabadi, R., Srolovitz, D. J. & Lesar, R. Segregation to and structure of [001] twist grain boundaries in Cu Ni alloys. *Acta Metall. Mater.* **41**, 2533–2546 (1993).
48. Wang, H. Y., Najafabadi, R., Srolovitz, D. J. & Lesar, R. Interfacial segregation in Ag-Au, Au-Pd, and Cu-Ni alloys: II. [001]  $\Sigma 5$  twist grain boundaries. *Interface Sci.* **1**, 31–47 (1993).
49. Scheiber, D., Popov, M. N. & Romaner, L. Temperature dependence of solute segregation energies at W GBs from first principles. *Scr. Mater.* **222**, 115059 (2023).
50. Řehák, P., Všíanská, M. & Černý, M. Role of vibrational entropy in impurity segregation at grain boundaries in bcc iron. *Comput. Mater. Sci.* **216**, 111858 (2023).
51. Tuchinda, N. & Schuh, C. A. The vibrational entropy spectra of grain boundary segregation in polycrystals. *Acta Mater.* **245**, 118630 (2023).
52. Rickman, J. M. & Srolovitz, D. J. A modified-local-harmonic model for solids. *Philos. Mag. A* **67**, 1081–1094 (1993).
53. LeSar, R., Najafabadi, R. & Srolovitz, D. J. Finite-temperature defect properties from free-energy minimization. *Phys. Rev. Lett.* **63**, 624–627 (1989).
54. Bartók, A. P., Payne, M. C., Kondor, R. & Csányi, G. Gaussian approximation potentials: the accuracy of quantum mechanics, without the electrons. *Phys. Rev. Lett.* **104**, 136403 (2010).
55. Bartók, A. P., Kondor, R. & Csányi, G. On representing chemical environments. *Phys. Rev. B* **87**, 184115 (2013).
56. Sheng, H. Al-Ag EAM Potential, Private communication. <https://sites.google.com/site/eampotentials/AlAg> (2012).
57. Adams, J. B., Foiles, S. M. & Wolfer, W. G. Self-diffusion and impurity diffusion of fee metals using the five-frequency model and the Embedded Atom Method. *J. Mater. Res.* **4**, 102–112 (1989).
58. Foiles, S. M., Baskes, M. I. & Daw, M. S. Embedded-atom-method functions for the fcc metals Cu, Ag, Au, Ni, Pd, Pt, and their alloys. *Phys. Rev. B* **33**, 7983–7991 (1986).
59. Fujita, T. et al. Coupling between chemical and dynamic heterogeneities in a multicomponent bulk metallic glass. *Phys. Rev. B* **81**, 140204 (2010).
60. Williams, P. L., Mishin, Y. & Hamilton, J. C. An embedded-atom potential for the Cu–Ag system. *Model. Simul. Mater. Sci. Eng.* **14**, 817 (2006).
61. Wu, H. H. & Trinkle, D. R. Cu/Ag EAM potential optimized for heteroepitaxial diffusion from ab initio data. *Comput. Mater. Sci.* **47**, 577–583 (2009).
62. Pan, Z., Borovikov, V., Mendeleev, M. I. & Sansoz, F. Development of a semi-empirical potential for simulation of Ni solute segregation into grain boundaries in Ag. *Model. Simul. Mater. Sci. Eng.* **26**, 075004 (2018).
63. Farkas, D. & Caro, A. Model interatomic potentials for Fe–Ni–Cr–Co–Al high-entropy alloys. *J. Mater. Res.* **35**, 3031–3040 (2020).
64. Purja Pun, G. P., Yamakov, V. & Mishin, Y. Interatomic potential for the ternary Ni–Al–Co system and application to atomistic modeling of the B2–L1<sub>0</sub> martensitic transformation. *Model. Simul. Mater. Sci. Eng.* **23**, 065006 (2015).
65. Cheng, Y. Q., Ma, E. & Sheng, H. W. Atomic level structure in multicomponent bulk metallic glass. *Phys. Rev. Lett.* **102**, 245501 (2009).
66. Liu, X.-Y., Liu, C.-L. & Borucki, L. J. A new investigation of copper’s role in enhancing Al–Cu interconnect electromigration resistance from an atomistic view. *Acta Mater.* **47**, 3227–3231 (1999).
67. Mendeleev, M. I., Srolovitz, D. J., Ackland, G. J. & Han, S. Effect of Fe segregation on the migration of a non-symmetric  $\Sigma 5$  tilt grain boundary in Al. *J. Mater. Res.* **20**, 208–218 (2005).
68. Liu, X.-Y., Ohotnicky, P. P., Adams, J. B., Rohrer, C. L. & Hyland, R. W. Anisotropic surface segregation in Al Mg alloys. *Surf. Sci.* **373**, 357–370 (1997).
69. Liu, X.-Y. & Adams, J. B. Grain-boundary segregation in Al–10%Mg alloys at hot working temperatures. *Acta Mater.* **46**, 3467–3476 (1998).
70. Mendeleev, M. I., Asta, M., Rahman, M. J. & Hoyt, J. J. Development of interatomic potentials appropriate for simulation of solid–liquid interface properties in Al–Mg alloys. *Philos. Mag.* **89**, 3269–3285 (2009).
71. Mishin, Y., Mehl, M. J. & Papaconstantopoulos, D. A. Embedded-atom potential for B 2 – NiAl. *Phys. Rev. B* **65**, 224114 (2002).
72. Mishin, Y. Atomistic modeling of the  $\gamma$  and  $\gamma'$ -phases of the Ni–Al system. *Acta Mater.* **52**, 1451–1467 (2004).
73. Purja Pun, G. P. & Mishin, Y. Development of an interatomic potential for the Ni–Al system. *Philos. Mag.* **89**, 3245–3267 (2009).
74. Landa, A. et al. Development of glue-type potentials for the Al–Pb system: phase diagram calculation. *Acta Mater.* **48**, 1753–1761 (2000).
75. Mendeleev, M. I. et al. Development of interatomic potentials appropriate for simulation of devitrification of Al90Sm10 alloy. *Model. Simul. Mater. Sci. Eng.* **23**, 045013 (2015).
76. Song, H. & Mendeleev, M. I. Molecular dynamics study of mechanism of solid–liquid interface migration and defect formation in Al3Sm alloy. *JOM* **73**, 2312–2319 (2021).
77. Farkas, D. & Jones, C. Interatomic potentials for ternary Nb – Ti – Al alloys. *Model. Simul. Mater. Sci. Eng.* **4**, 23–32 (1996).
78. Zope, R. R. & Mishin, Y. Interatomic potentials for atomistic simulations of the Ti–Al system. *Phys. Rev. B* **68**, 024102 (2003).
79. Deluigi, O. R. et al. Simulations of primary damage in a High Entropy Alloy: probing enhanced radiation resistance. *Acta Mater.* **213**, 116951 (2021).
80. Farkas, D. & Caro, A. Model interatomic potentials and lattice strain in a high-entropy alloy. *J. Mater. Res.* **33**, 3218–3225 (2018).
81. Bonny, G., Pasianot, R. C., Castin, N. & Malerba, L. Ternary Fe–Cu–Ni many-body potential to model reactor pressure vessel steels: First validation by simulated thermal annealing. *Philos. Mag.* **89**, 3531–3546 (2009).
82. Fischer, F., Schmitz, G. & Eich, S. M. A systematic study of grain boundary segregation and grain boundary formation energy using a new copper–nickel embedded-atom potential. *Acta Mater.* **176**, 220–231 (2019).
83. Foiles, S. M. Calculation of the surface segregation of Ni–Cu alloys with the use of the embedded-atom method. *Phys. Rev. B* **32**, 7685–7693 (1985).
84. Onat, B. & Durukanoglu, S. An optimized interatomic potential for Cu–Ni alloys with the embedded-atom method. *J. Phys. Condens. Matter* **26**, 035404 (2013).
85. Hoyt, J. J., Garvin, J. W., Webb, E. B. & Asta, M. An embedded atom method interatomic potential for the Cu Pb system. *Model. Simul. Mater. Sci. Eng.* **11**, 287–299 (2003).
86. Borovikov, V., Mendeleev, M. I. & King, A. H. Effects of stable and unstable stacking fault energy on dislocation nucleation in nano-crystalline metals. *Model. Simul. Mater. Sci. Eng.* **24**, 085017 (2016).
87. Cheng, Y. Q., Sheng, H. W. & Ma, E. Relationship between structure, dynamics, and mechanical properties in metallic glass-forming alloys. *Phys. Rev. B* **78**, 014207 (2008).
88. Mendeleev, M. I., Sordelet, D. J. & Kramer, M. J. Using atomistic computer simulations to analyze x-ray diffraction data from metallic glasses. *J. Appl. Phys.* **102**, 043501 (2007).



89. Mendeleev, M. I. et al. Development of suitable interatomic potentials for simulation of liquid and amorphous Cu–Zr alloys. *Philos. Mag.* **89**, 967–987 (2009).
90. Baskes, M. I., Sha, X., Angelo, J. E. & Moody, N. R. Trapping of hydrogen to lattice defects in nickel. *Model. Simul. Mater. Sci. Eng.* **5**, 651 (1997).
91. Béland, L. K. et al. Features of primary damage by high energy displacement cascades in concentrated Ni-based alloys. *J. Appl. Phys.* **119**, 085901 (2016).
92. Li, Q.-J., Sheng, H. & Ma, E. Strengthening in multi-principal element alloys with local-chemical-order roughened dislocation pathways. *Nat. Commun.* **10**, 3563 (2019).
93. Béland, L. K. et al. Accurate classical short-range forces for the study of collision cascades in Fe–Ni–Cr. *Comput. Phys. Commun.* **219**, 11–19 (2017).
94. Bonny, G., Terentyev, D., Pasianot, R. C., Poncé, S. & Bakaev, A. Interatomic potential to study plasticity in stainless steels: the FeNiCr model alloy. *Model. Simul. Mater. Sci. Eng.* **19**, 085008 (2011).
95. Bonny, G., Castin, N. & Terentyev, D. Interatomic potential for studying ageing under irradiation in stainless steels: the FeNiCr model alloy. *Model. Simul. Mater. Sci. Eng.* **21**, 085004 (2013).
96. Zhou, X. W., Foster, M. E. & Sills, R. B. An Fe–Ni–Cr embedded atom method potential for austenitic and ferritic systems. *J. Comput. Chem.* **39**, 2420–2431 (2018).
97. Zhang, Y., Ashcraft, R., Mendeleev, M. I., Wang, C. Z. & Kelton, K. F. Experimental and molecular dynamics simulation study of structure of liquid and amorphous Ni<sub>62</sub>Nb<sub>38</sub> alloy. *J. Chem. Phys.* **145**, 204505 (2016).
98. Samolyuk, G. D., Béland, L. K., Stocks, G. M. & Stoller, R. E. Electron–phonon coupling in Ni-based binary alloys with application to displacement cascade modeling. *J. Phys. Condens. Matter* **28**, 175501 (2016).
99. Sheng, H. W., Ma, E. & Kramer, M. J. Relating dynamic properties to atomic structure in metallic glasses. *JOM* **64**, 856–881 (2012).
100. Kong, L. T., Liu, J. B., Lal, W. S. & Liu, B. X. Correlation of lattice constant versus tungsten concentration of the Ni-based solid solution examined by molecular dynamics simulation. *J. Alloy. Compd.* **337**, 143–147 (2002).
101. Mendeleev, M. I., Kramer, M. J., Hao, S. G., Ho, K. M. & Wang, C. Z. Development of interatomic potentials appropriate for simulation of liquid and glass properties of NiZr<sub>2</sub> alloy. *Philos. Mag.* **92**, 4454–4469 (2012).
102. Wilson, S. R. & Mendeleev, M. I. Anisotropy of the solid–liquid interface properties of the Ni–Zr B33 phase from molecular dynamics simulation. *Philos. Mag.* **95**, 224–241 (2015).
103. Azzalini, A. & Capitanio, A. Statistical applications of the multivariate skew normal distribution. *J. R. Stat. Soc. Ser. B Stat. Methodol.* **61**, 579–602 (1999).
104. Azzalini, A. *The R Package ‘Sn’: The Skew-Normal and Related Distributions Such as the Skew-t and the SUN (Version 2.0.2)*. (Università degli Studi di Padova, 2022).
105. Zhao, L., Najafabadi, R. & Srolovitz, D. J. Finite temperature vacancy formation thermodynamics: local harmonic and quasiharmonic studies. *Model. Simul. Mater. Sci. Eng.* **1**, 539–551 (1993).
106. Lejček, P. & Hofmann, S. Thermodynamics of grain boundary segregation and applications to anisotropy, compensation effect and prediction. *Crit. Rev. Solid State Mater. Sci.* **33**, 133–163 (2008).
107. Schönbrodt, F. D. & Perugini, M. At what sample size do correlations stabilize? *J. Res. Personal.* **47**, 609–612 (2013).
108. Tuchinda, N. & Schuh, C. A. Dataset - Computed Entropy Spectra for Grain Boundary Segregation in Polycrystals. figshare <https://doi.org/10.6084/m9.figshare.24132267>.
109. Freitas, R. & Cao, Y. Machine-learning potentials for crystal defects. *MRS Commun.* 1–11 (2022).
110. Matsuura, M., Yokoi, T., Ogura, Y. & Matsunaga, K. Anharmonicity in grain boundary energy for Al: Thermodynamic integration with artificial-neural-network potential. *Scr. Mater.* **236**, 115685 (2023).
111. Kalidindi, A. R. & Schuh, C. A. Stability criteria for nanocrystalline alloys. *Acta Mater.* **132**, 128–137 (2017).
112. Wagih, M. & Schuh, C. A. Thermodynamics and design of nanocrystalline alloys using grain boundary segregation spectra. *Acta Mater.* **217**, 117177 (2021).
113. Seki, A., Seidman, D. N., Oh, Y. & Foiles, S. M. Monte Carlo simulations of segregation at [001] twist boundaries in a Pt(Au) alloy —II. Discussion. *Acta Metall. Mater.* **39**, 3179–3185 (1991).
114. Seki, A., Seidman, D. N., Oh, Y. & Foiles, S. M. Monte Carlo simulations of segregation at [001] twist boundaries in a Pt(Au) alloy —I. Results. *Acta Metall. Mater.* **39**, 3167–3177 (1991).
115. Lejček, P., Hofmann, S., Všianská, M. & Šob, M. Entropy matters in grain boundary segregation. *Acta Mater.* **206**, 116597 (2021).
116. Lejček, P. & Hofmann, S. On the relationship between entropy and enthalpy of grain boundary segregation. *Interface Sci.* **9**, 221–230 (2001).
117. Suzuki, S. Influence of a variety of grain boundary structures on grain boundary segregation. *Isij Int.* **30**, 1000–1002 (1990).
118. Mütschele, T. & Kirchheim, R. Segregation and diffusion of hydrogen in grain boundaries of palladium. *Scr. Metall.* **21**, 135–140 (1987).
119. Seidman, D. N. Solute-atom segregation at internal interfaces on an atomic scale: atom-probe experiments and computer simulations. *Mater. Sci. Eng. A* **137**, 57–67 (1991).
120. Barr, C. M. et al. The role of grain boundary character in solute segregation and thermal stability of nanocrystalline Pt–Au. *Nanoscale* **13**, 3552–3563 (2021).
121. Lu, P. et al. On the thermal stability and grain boundary segregation in nanocrystalline PtAu alloys. *Materialia* **6**, 100298 (2019).
122. Paine, D. C., Weatherly, G. C. & Aust, K. T. A STEM study of grain-boundary segregation in Al-6.5 wt% Mg alloy. *J. Mater. Sci.* **21**, 4257–4261 (1986).
123. Vatter, I. A. & Titchmarsh, J. M. Measurement of grain-boundary segregation by STEM-EDX analysis. *Ultramicroscopy* **28**, 236–239 (1989).
124. Meiners, T., Frolov, T., Rudd, R. E., Dehm, G. & Liebscher, C. H. Observations of grain-boundary phase transformations in an elemental metal. *Nature* **579**, 375–378 (2020).
125. Frolov, T., Olmsted, D. L., Asta, M. & Mishin, Y. Structural phase transformations in metallic grain boundaries. *Nat. Commun.* **4**, 1899 (2013).
126. Freitas, R., Rudd, R. E., Asta, M. & Frolov, T. Free energy of grain boundary phases: Atomistic calculations for  $\Sigma$  5 (310) [001] grain boundary in Cu. *Phys. Rev. Mater.* **2**, 093603 (2018).
127. Luo, J., Gupta, V. K., Yoon, D. H. & Meyer, H. M. Segregation-induced grain boundary premelting in nickel-doped tungsten. *Appl. Phys. Lett.* **87**, 231902 (2005).
128. Luo, J. Grain boundary complexions: the interplay of premelting, prewetting, and multilayer adsorption. *Appl. Phys. Lett.* **95**, 071911 (2009).
129. Cantwell, P. R. et al. Grain boundary complexions. *Acta Mater.* **62**, 1–48 (2014).
130. Rohrer, G. S. The role of grain boundary energy in grain boundary complexion transitions. *Curr. Opin. Solid State Mater. Sci.* **20**, 231–239 (2016).
131. Fowler, S. R. H. & Guggenheim, E. A. *Statistical Thermodynamics. A Version of Statistical Mechanics [by RH Fowler] for Students of Physics and Chemistry*. (Cambridge, 1939).
132. Matson, T. P. & Schuh, C. A. Atomistic assessment of solute-solute interactions during grain boundary segregation. *Nanomaterials* **11**, 2360 (2021).
133. Wagih, M., Larsen, P. M. & Schuh, C. A. Dataset—learning grain boundary segregation energy spectra in polycrystals. *Zenodo* <https://doi.org/10.5281/zenodo.4107058> (2020).

134. Bitzek, E., Koskinen, P., Gähler, F., Moseler, M. & Gumbusch, P. Structural relaxation made simple. *Phys. Rev. Lett.* **97**, 170201 (2006).
135. Guérolé, J. et al. Assessment and optimization of the fast inertial relaxation engine (fire) for energy minimization in atomistic simulations and its implementation in lammmps. *Comput. Mater. Sci.* **175**, 109584 (2020).
136. Plimpton, S. Fast parallel algorithms for short-range molecular dynamics. *J. Comput. Phys.* **117**, 1–19 (1995).
137. Brown, W. M., Wang, P., Plimpton, S. J. & Tharrington, A. N. Implementing molecular dynamics on hybrid high performance computers—short range forces. *Comput. Phys. Commun.* **182**, 898–911 (2011).
138. Brown, W. M., Kohlmeyer, A., Plimpton, S. J. & Tharrington, A. N. Implementing molecular dynamics on hybrid high performance computers—Particle—particle mesh. *Comput. Phys. Commun.* **183**, 449–459 (2012).
139. Brown, W. M. & Yamada, M. Implementing molecular dynamics on hybrid high performance computers—three-body potentials. *Comput. Phys. Commun.* **184**, 2785–2793 (2013).
140. Pearson, K. & Lill. On lines and planes of closest fit to systems of points in space. *Lond. Edinb. Dublin Philos. Mag. J. Sci.* **2**, 559–572 (1901).
141. Hotelling, H. Analysis of a complex of statistical variables into principal components. *J. Educ. Psychol.* **24**, 417 (1933).
142. Tipping, M. E. & Bishop, C. M. Probabilistic principal component analysis. *J. R. Stat. Soc. Ser. B Stat. Methodol.* **61**, 611–622 (1999).
143. Lloyd, S. Least squares quantization in PCM. *IEEE Trans. Inf. Theory* **28**, 129–137 (1982).
144. Elkan, C. Using the triangle inequality to accelerate k-means. In *Proceedings of the 20th international conference on Machine Learning (ICML-03)* 147–153 (2003).
145. Honeycutt, J. D. & Andersen, H. C. Molecular dynamics study of melting and freezing of small Lennard-Jones clusters. *J. Phys. Chem.* **91**, 4950–4963 (1987).
146. Stukowski, A. Structure identification methods for atomistic simulations of crystalline materials. *Model. Simul. Mater. Sci. Eng.* **20**, 045021 (2012).
147. Stukowski, A. Visualization and analysis of atomistic simulation data with OVITO—the Open Visualization Tool. *Model. Simul. Mater. Sci. Eng.* **18**, 015012 (2009).
148. Sievers, C. A. *Thermal Transport in 2D Materials* (UC Davis, 2021).
149. Li, Z. et al. Influence of thermostatting on nonequilibrium molecular dynamics simulations of heat conduction in solids. *J. Chem. Phys.* **151**, 234105 (2019).
150. Kluyver, T. et al. Jupyter Notebooks – a publishing format for reproducible computational workflows. In *Positioning and Power in Academic Publishing: Players, Agents and Agendas* (eds. Loizides, F. & Schmidt, B.) 87–90 (IOS Press, 2016).
151. Harris, C. R. et al. Array programming with NumPy. *Nature* **585**, 357–362 (2020).
152. Virtanen, P. et al. SciPy 1.0: fundamental algorithms for scientific computing in Python. *Nat. Methods* **17**, 261–272 (2020).
153. Piessens, R., de Doncker-Kapenga, E., Überhuber, C. W. & Kahaner, D. K. *Quadpack: A Subroutine Package for Automatic Integration*. vol. 1 (Springer Science & Business Media, 2012).
154. Brent, R. P. *Algorithms for Minimization without Derivatives* (Courier Corporation, 2013).
155. Hunter, J. D. Matplotlib: a 2D graphics environment. *Comput. Sci. Eng.* **9**, 90–95 (2007).
156. Joblib Development Team. Joblib: running Python functions as pipeline jobs. (2022).
157. Waskom, M. L. Seaborn: statistical data visualization. *J. Open Source Softw.* **6**, 3021 (2021).
158. Pedregosa, F. et al. Scikit-learn: Machine Learning in Python. *Mach. Learn. PYTHON* **6**.
159. da Costa-Luis, C. et al. tqdm: A fast, Extensible Progress Bar for Python and CLI. *Zenodo* (2021).
160. Ishida, K. Effect of grain size on grain boundary segregation. *J. Alloy. Compd.* **235**, 244–249 (1996).
161. Palumbo, G., Thorpe, S. J. & Aust, K. T. On the contribution of triple junctions to the structure and properties of nanocrystalline materials. *Scr. Metall. Mater.* **24**, 1347–1350 (1990).
162. Lejček, P. *Grain Boundary Segregation in Metals* Vol. 136 (Springer Berlin Heidelberg, 2010).
163. Lejček, P. & Hofmann, S. Interstitial and substitutional solute segregation at individual grain boundaries of  $\alpha$ -iron: data revisited. *J. Phys. Condens. Matter* **28**, 064001 (2016).

## Acknowledgements

Work on data science and learning of GB segregation parameters was supported by the US Department of Energy award No. DE-SC0020180. Work on the development of entropy calculation methods was supported by the U.S. National Science Foundation under Grant No. DMR 2002860. The authors acknowledge MIT Satori and Research Computing Project for the computational resources used in this work. N.T. acknowledges the financial support from Anandamahidol Foundation Scholarship and fruitful discussions with M. Wagih and T. Matson at MIT.

## Author contributions

N.T. developed the methodology and performed the calculations, C.A.S. supervised the project. Both authors contributed in analyzing the results and in the writing of the manuscript.

## Competing interests

The authors declare no competing interests.

## Additional information

**Supplementary information** The online version contains supplementary material available at <https://doi.org/10.1038/s41524-024-01260-3>.

**Correspondence** and requests for materials should be addressed to Christopher A. Schuh.

**Reprints and permissions information** is available at <http://www.nature.com/reprints>

**Publisher's note** Springer Nature remains neutral with regard to jurisdictional claims in published maps and institutional affiliations.

**Open Access** This article is licensed under a Creative Commons Attribution 4.0 International License, which permits use, sharing, adaptation, distribution and reproduction in any medium or format, as long as you give appropriate credit to the original author(s) and the source, provide a link to the Creative Commons licence, and indicate if changes were made. The images or other third party material in this article are included in the article's Creative Commons licence, unless indicated otherwise in a credit line to the material. If material is not included in the article's Creative Commons licence and your intended use is not permitted by statutory regulation or exceeds the permitted use, you will need to obtain permission directly from the copyright holder. To view a copy of this licence, visit <http://creativecommons.org/licenses/by/4.0/>.

© The Author(s) 2024